Journal of the European Ceramic Society 22 (2002) 2677–2687
www.elsevier.com/locate/jeurceramsoc

X-ray line-broadening study of a liquid-phase-sintered silicon carbide

A.L. Ortiz[a,*], F. Sánchez-Bajo[a], A. Hernández-Jiménez[a], F. Guiberteau[a], F.L. Cumbrera[b]

[a]*Departamento de Electrónica e Ingeniería Electromecánica, Escuela de Ingenierías Industriales, Universidad de Extremadura, 06071 Badajoz, Spain*
[b]*Departamento de Física, Facultad de Ciencias, Universidad de Extremadura, 06071 Badajoz, Spain*

Received 29 October 2001; received in revised form 10 January 2002; accepted 30 January 2002

Abstract

Silicon carbide (SiC), owing to its unique combination of chemical and physical properties, is the material of choice for advanced engineering applications both at room and high temperatures. Due to the difficulty of SiC to be solid-state sintered, nowadays there has been growing interest in liquid-phase sintering (LPS) of SiC. Here, there is a critical need for developing methodologies for the accurate X-ray diffraction characterization of the microstructures of these ceramics as their microstructural evolution is not yet totally understood. Thus, the aim of the present work is to apply a procedure for the accurate line-broadening study of any given phase in LPS SiC ceramics. To that end, we have pressureless liquid-phase sintered (at 1950 °C for 0.5 h in flowing Ar atmosphere) a specimen starting from a commercially available β-SiC powder and using the simultaneous addition of Al_2O_3 and Y_2O_3. The resulting material was subsequently characterized using X-ray powder diffraction; more specifically, the Rietveld method was applied for the quantitative phase-composition analysis and the Warren–Averbach method for determining the mean crystallite size, the crystallite size distribution and the root-mean-square strain along the crystallographic direction $<111>$ of the β-SiC polytype. The nanometric nature of the crystallite size distribution is finally related with the stacking faults in the SiC starting powder.

Keywords: Line-broadening analysis; Quantitative phase-composition analysis; SiC; X-ray powder diffraction

1. Introduction

In the context of structural ceramics for high temperature applications there is a growing interest in developing new silicon carbide (SiC) based ceramics. Here, SiC is preferred over other ceramics because it offers some advantages in terms of chemical and physical properties. However, the major drawback of SiC resides in its difficulty to be solid-state sintered, primarily due to the inherently covalent nature of the bonding. For this reason, nowadays more and more SiC-based ceramics are being fabricated through liquid-phase sintering. However, although liquid-phase sintering offers some unique advantages and possibilities to manufacture covalent ceramics, widespread application of this processing routine to SiC has been surprisingly sparse. The principal stumbling-block for the commercial exploitation of liquid-phase-sintered (LPS) SiC is the lack of scientific understanding of microstructural evolution during sintering. It is reasonable to think that one of the major reasons is that SiC exhibits polytypism; of course, accurate quantitative-polytype composition analyses and exhaustive measurements of the crystallite size of the different polytypes are essential for understanding the microstructural development and most of the properties in SiC-based ceramics. Here, X-ray diffraction (XRD) is recognized to be the most valuable and suitable analytical technique for performing such measurements. Unfortunately, XRD characterization of SiC-based microstructures is far away from being trivial primarily because of the significant overlap between the Bragg reflections from the different polytypes. However, it has been recently shown that the overlapping Bragg reflections problem is overcame if the

* Corresponding author. Tel.: +34-924-289600; fax: +34-924-289601.
E-mail address: alortiz@unex.es (A.L. Ortiz).

0955-2219/02/$ - see front matter
PII: S0955-2219(02)00133-4

Rietveld method is used for analyzing the experimental XRD patterns.[1–4] Also, the Rietveld method has been applied in conjunction with the variance and integral-breadth methods for carrying out accurate measurements of the mean diffraction domain size for the polytypes present in a LPS SiC ceramic.[5] However, although the mean crystallite size is an important microstructural parameter, sometimes a more detailed microstructural information such as the accurate measurement of the crystallite size distribution is needed in order to explain the behavior of the material. Again, XRD should be the method of choice.

The aim of the present work is to present a procedure for the accurate line-broadening study in LPS SiC ceramics. To that end, we have used the Rietveld method[6,7] in conjunction with the Warren–Averbach method[8,9] for determining the relative amount of the different phases and obtaining the crystallite size distribution of the β-SiC (3C) polytype along its $<111>$ crystallographic direction. Although we simply point out here a methodology (any other intend was behind the scope of this paper), it is anticipated that its systematic use could give insight for a better understanding of the microstructural development in LPS SiC ceramics. Thus, the broader goal of using this procedure for studying the microstructural evolution (that is, working on samples sintered at different times, atmospheres, starting SiC powders, additives, etc.) in this high performance material is delayed for a near future.

2. Fundamental concepts of the XRD characterization

2.1. The Rietveld method

It is known that many Bragg reflections can contribute to the observed intensity, y_i^{OBS}, at the ith step (in the step-scanning mode) in the XRD pattern. Thus, in the Rietveld method, the calculated intensity, y_i^{CAL}, at that point is determined from the structural and the profile models plus the background contribution. A non-linear least-squares refinement is carried out until the best fit is obtained between the entire observed XRD pattern taken as a whole and the entire calculated XRD pattern based on the following equation:[7]

$$y_i^{CAL} = b_i + \sum_j S_j \sum_g M_{jg}\, LP_{jg}\, F_{jg}^2\; A_{jg}\; \Omega_{jg}(2\theta_i - 2\theta_{jg}), \quad (1)$$

where b_i represents the background intensity at the ith step, and the double summation represents the structural and the profile models. Here, the subscript j refers to the different crystalline phases, while the subscript g refers to the Miller indices (which are h, k, and l) for the Bragg reflections. The term S_j in Eq. (1) represents the Rietveld scale factor for the jth phase, while the terms M_{jg}, LP_{jg}, F_{jg} and A_{jg} are (for the gth reflection of the jth phase) the multiplicity, the Lorentz-polarization factor, the structure factor and a function that takes into account absorption and/or texture effects, respectively. Finally, Ω_{jg} is the reflection profile function (normalized to unit area and with maximum at $2\theta_{jg}$) which approximates the effects of both instrumental and sample features (such as diffraction domain sizes and lattice microstrains). Therefore, it can be seen that the model parameters that may be refined include not only atomic positions, thermal and site-occupancy factors, but also parameters for the background, lattice, instrumental geometrical-optical features, and specimen reflection-profile-broadening agents. Multiple phases may be refined simultaneously and comparative analysis of the separate overall Rietveld scale factor for the phases offers what is probably the most reliable method for performing quantitative phase-composition analysis.[7] In this regard, the weight fraction of the jth phase (X_j) can be obtained using the following equation:[10–12]

$$X_j = \frac{S_j Z_j M_j V_j}{\sum_j S_j Z_j M_j V_j}, \quad (2)$$

where S_j, Z_j, M_j and V_j are the Rietveld scale factor, the number of formula units per unit cell, the formula unit molecular weight, and the unit cell volume of the jth phase, respectively, and the index j in the summation is over all phases included in the model.

Of course, some criteria of fit or profile agreement indexes are needed to judge whether or not the refinement proceeded satisfactorily. Here we have used the weighted pattern index R_{wp} and the reduced chi-square χ_r^2 (also denoted as the goodness of fit), which are defined as:

$$R_{wp} = 100 \sqrt{\frac{\sum_i w_i \left(y_i^{OBS} - y_i^{CAL}\right)^2}{\sum_i w_i \left(y_i^{OBS}\right)^2}} \quad (3)$$

and

$$\chi_r^2 = \frac{\sum_i w_i \left(y_i^{OBS} - y_i^{CAL}\right)^2}{N - P} \quad (4)$$

where the summations cover all points in the pattern. The quantities w_i are weight factors, which are defined as $w_i = 1/y_i^{OBS}$. The term N and P in Eq. (4) represent the total number of data points and the number of refined parameters, respectively. Although numerical criteria are very important, we also have used graphical criteria of fit, such as the difference plot as well as plots of the observed and calculated patterns.

2.2. The Warren–Averbach method

It is known from the kinematical XRD theory[9] that the observed X-ray profile $h(x)$ is the convolution of two functions: (1) a function $g(x)$ describing the spectral and instrumental effects, which is usually measured with a suitable standard sample and, (2) a function $f(x)$ describing the pure profile of the sample, which takes into account microstructural features such as crystallite sizes and lattice microstrains. This is mathematically expressed as follows:

$$h(x) = \int_{-\infty}^{+\infty} g(x-y) f(y) dy \tag{5}$$

which is a first-kind Fredholm linear integral equation. Of course, when dealing with the XRD microstructural characterization of materials, the experimental and spectral-instrumental functions are directly accessible from a good-conducted experiment and the main problem just reduces to determine the unknown pure profile. Unfortunately, although it is potentially possible to obtain the pure profile by the deconvolution of Eq. (5), this latter becomes a very difficult task in a real case due to its ill-posed nature. Thus, most of the early work centered on developing indirect procedures (such as the variance and integral-breadth methods) that, while avoiding the deconvolution of Eq. (5), still would led to obtain some representative parameters of the pure profile. The major inconvenient of these procedures is that the pure profile can not be subsequently restituted from that slanted information and, therefore, only some microstructural parameters such as the mean crystallite size and the root-mean-square strain $\sqrt{< e^2 >}$ can be obtained.

There is an alternative and elegant procedure for restituting the pure profile making use of the convolutive character of Eq. (5). This pushes us to describe both the experimental (Bragg reflection *hkl*) and instrumental profiles in term of their Fourier transforms $H_{hkl}(L)$ and $G(L)$; note that $H_{hkl}(L)$ and $G(L)$ are expressed as function of the distance L, which is measured perpendicularly to the diffracting plane family $\{hkl\}$. Once these Fourier transforms are known, the Fourier integral-convolution theorem can be applied for obtaining the unknown Fourier transform of the pure profile f, that is, the function $F_{hkl}(L)$. The key point here is that all the microstructural information contained in the pure profile $f(x)$ is also present in the real part of its corresponding Fourier transform $F_{hkl}(L)$, that is, in its Fourier cosine transform $F_{hkl,C}(L)$. This latter is the product of the two different components: (1) $F^S_{\{hkl\}}(L)$, which is a size component associated with the column length and; (2) $F^D_{hkl}(L)$, which is a microstrain component associated with the lattice distortion. The Warren–Averbach method is based on separating the size and distortion components using the Fourier cosine transform $F_{hkl,C}(L)$ of several orders of the *hkl* reflection. The procedure lies on the fact that $F^D_{hkl}(L)$ does depend upon the order of the *hkl* reflection whereas $F^S_{\{hkl\}}(L)$ is order-independent. Here, the Warren–Averbach method assumes that the distortion component can be approximated by a Gaussian function in the form:

$$F^D_{hkl}(L) \approx e^{-\frac{2\pi^2 L^2 < e_L^2 >}{d_{hkl}^2}} \tag{6}$$

where d_{hkl} is the interplanar distance and $\sqrt{< e_L^2 >}$ represents the root-mean-square strain averaged over L. Note that the logarithm of the Fourier cosine transform $F_{hkl,C}(L)$ is then given by the following expression:

$$Ln\, F_{hkl,C}(L) = Ln\left[F^S_{\{hkl\}}(L) \cdot F^D_{hkl}(L,d) \right] \approx Ln\, F^S_{\{hkl\}}(L) - \frac{2\pi^2 L^2 < e_L^2 >}{d_{hkl}^2} \tag{7}$$

So far, it has been assumed that several different orders of the *hkl* reflection can be experimentally collected; in most of the cases only two reflections are available and, therefore, we just limited ourselves to describe the application of the Warren–Averbach method in that particular situation. Thus, if $F_{1,C}(L)$ and $F_{2,C}(L)$ are the Fourier cosine transforms of the first and second reflections, the root-mean-square strain can be calculated from:

$$< e_L^2 > = \frac{\mathrm{Ln}\, F_{1,C}(L) - \mathrm{Ln}\, F_{2,C}(L)}{2\pi^2 L^2 \left(\frac{1}{d_2^2} - \frac{1}{d_1^2} \right)} \tag{8}$$

where d_1 and d_2 are the interplanar distances of diffracting planes associated with these Bragg reflections.

Once the value of $\sqrt{< e_L^2 >}$ is known as a function of L, Eq. (7) can be easily applied to determine the size component $F^S_{\{hkl\}}(L)$ of the cosine Fourier transform $F_{hkl,C}(L)$. After plotting $F^S_{\{hkl\}}(L)$ versus L, the mean crystallite size can be directly obtained from the abscissa intercept of the initial slope. Most importantly, the crystallite size distribution is related with the second derivative of $F^S_{\{hkl\}}(L)$ through the following expression:

$$p(L) \propto L \frac{\mathrm{d}^2 F^S_{\{hk\}}}{\mathrm{d}L^2} \tag{9}$$

3. Experimental procedure

3.1. Processing

Commercially available submicrometer powders of β-SiC (BF-12, H.C. Starck, Berlin, Goslar, Germany), Y_2O_3 (Fine Grade, H.C. Starck, Berlin, Goslar, Germany)

and Al_2O_3 (AKP-30, Sumitomo chemical Company, New York, NY) were used as starting materials. These powders were combined in the following proportion: 73.86 wt.% β-SiC, 14.92 wt.% Y_2O_3, and 11.22 wt.% Al_2O_3. The powder batch was blended intimately by wet-ball-milling in methanol for 24 h in a polyethylene bottle using zirconia balls. The resulting slurry was dried in a Teflon beaker on a hot-plate while being continuously stirred. The dried powder was then deagglomerated by crushing. Subsequently, approximately 10 g of the mixed powder were pressed uniaxially into a pellet (25 mm in diameter × 7 mm thick) at a pressure of 50 MPa in a graphite die, followed by cold isostatic pressing at 350 MPa. The individual pellet was then embedded in powder beds inside a graphite crucible with screwable lid. Typical powder bed composition consisted of 90 wt.% SiC and 10 wt.% Al_2O_3. The pellet was then sintered isothermally in a graphite furnace at a temperature of 1950 °C for 0.5 h in flowing Ar atmosphere. After removing it from the furnace, the pellet was cleaned and its surface was ground off to remove the extraneous powder that was sticking to the sample. The ground sample was then crushed in a mortar and pestle to obtain a powder for X-ray diffraction characterization.

3.2. X-ray diffraction characterization

The XRD pattern of the LPS SiC specimen was obtained using a Philips PW-1800 diffractometer (Philips Research Laboratories, Eindhoven, The Netherlands) with CuK_α radiation (at a wavelength of $\lambda = 1.54183$ Å) and a graphite secondary monochromator. The generator settings were 40 kV and 35 mA. In a first experiment, the diffraction data were collected over a 2θ range of 20–100°, with a step of 0.05° and a counting time of 5 s per step. These XRD data were analyzed using the Rietveld refinement method to obtain the phase composition. In this study the Rietveld refinements were performed using the version 3.1 of the Rietveld analysis program FULLPROF, where the peak shape was assumed to be a pseudo-Voigt function. In addition, the conventional refinement protocol, which takes into account structural, profile and global parameters, included: (1) the background, which was modeled as a third-order polynomial function; (2) the Rietveld scale factors; (3) the global instrumental parameters (zero-point $2\theta_o$ shift and systematic shifts depending on the transparency and off-centering of the sample); (4) the lattice parameters for all phases and; (5) the profile parameters for all phases (Caglioti half-width parameters[13] U, V and W and the mixing parameter—η—of the pseudo-Voigt function).

In a second and more detailed experiment, the diffraction data were collected over the 2θ ranges of 35.2–36.4° and 74.5–76.2°, with a step of 0.01° and counting times of 10 and 20 s per step, respectively. Subsequently, a Levenberg–Marquardt non-linear least-squares fit (LM-fit) was used for modeling analytical functions to these XRD data. Here, we have assumed again pseudo-Voigt functions to describe the shape of the XRD peaks, which included Cu$K_{\alpha 1}$ and Cu$K_{\alpha 2}$ incident radiation components. In addition, the LM-fits included parameters describing a linear background, peak heights (I_0), positions of the maximum peak intensities ($2\theta_0$), peak half-widths at half-maxima (ω) and mixing parameters (η) of the pseudo-Voigt functions. The parameters (I_0, $2\theta_0$, ω and η) describing these pseudo-Voigt functions were then used in the line-broadening microstructural analysis.

In a third experiment, we have collected the instrumental peaks in 2θ positions close to the 111 and 222 Bragg reflections of the 3C polytype. These instrumental lines were obtained from the XRD pattern of an α-Al_2O_3 standard specimen. This standard sample was prepared by heating commercially available α-Al_2O_3 powders (99.99%, 1 μm, APS, Alfa, USA) in air at a temperature of 1500 °C for 8 h. Subsequently, the diffraction data were collected over the 2θ ranges of 34.5–36.0° and 76.2–77.8°, with a step of 0.01° and a counting time of 10 s per step. Again, the same LM-fit was used for modeling analytical functions to these XRD data, but this time using split pseudo-Voigt functions due to the inherently asymmetric nature of the instrumental peaks.

Finally, the XRD pattern of the SiC starting powder was also acquired with a step of 0.05° and a counting time of 5 s per step, but this time over the 2θ range of 30–45°.

3.3. Transmission electron microscopy (TEM) characterization

TEM specimens were prepared from the starting SiC powder using standard procedures for ceramics powders. Thus, 5 vol.% powders were suspended in methanol and subsequently dispersed during 40 min in an ultrasonic mixer. Then, TEM specimens were prepared by capturing powder particles on a 200 mesh size TEM copper grid by dipping in dilute particulate suspension. These specimens were then observed in a conventional TEM (Model EM420, Philips Electron Optics, Eindhoven, The Netherlands) operated at 100 KeV. The TEM micrographs were obtained by tilting the specimen such that the beam was along the [011] zone axis for cubic SiC.

4. Results and discussion

Fig. 1a shows the XRD pattern of the β-SiC starting powder used in this study for sintering our advanced

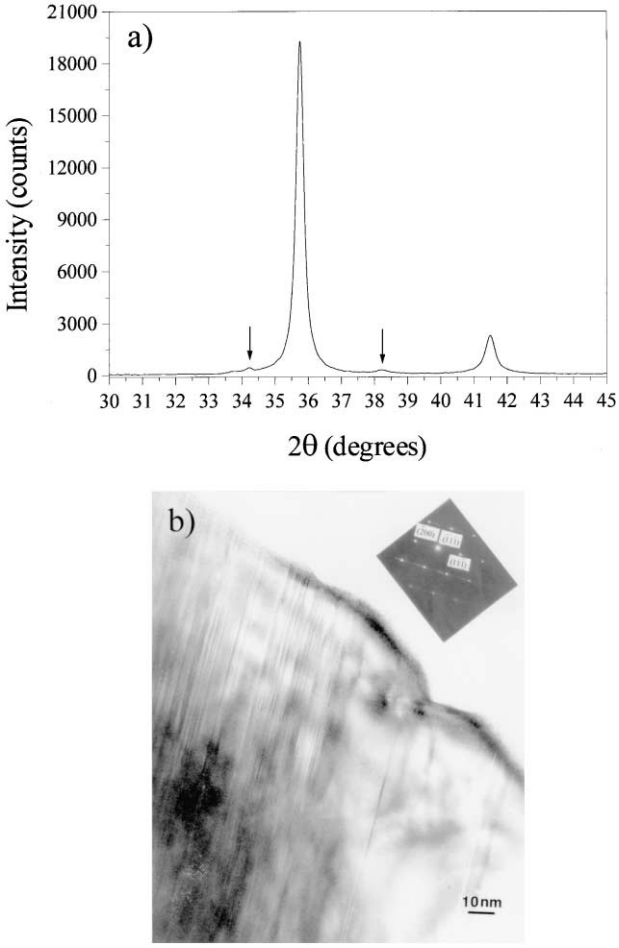

Fig. 1. X-ray diffraction pattern in the 2θ range 30–45° of the β-SiC starting powder (a) and bright-field transmission electron microscopy micrograph of a representative β-SiC particle, imaged along [011] zone axis, with the corresponding electron diffraction pattern inserted (b). Arrows in (a) denote extra peaks at $2\theta = 34.2°$ and 38.2°.

ceramic. The following interesting features can be observed: (1) the peak broadening (more remarkable in the 111 peak); (2) the undulations in the background intensities and; (3) the extra peaks at $2\theta \approx 34.2°$ and $2\theta \approx 38.2°$. These deviations from the ideal XRD pattern of the 3C polytype has been already attributed to planar defects (stacking faults and microtwins).[14] Fig. 1b shows a bright-field TEM micrograph of a representative β-SiC powder particle and the corresponding electron diffraction pattern. Observe the presence of planar defects and the attendant streaking of the diffraction spots. Thus, the earlier figures clearly demonstrate that the starting particle is uniquely formed by the 3C polytype, although it contains a multitude of different diffraction domains.

Fig. 2 shows the XRD pattern of the LPS SiC sample. Qualitative phase-identification analysis of the XRD pattern in Fig. 2 shows that the specimen contents the 4H and 6H polytypes, as well as the YAG and $YAlO_3$ phases. The presence of the β-SiC polytype could not be confirmed in the XRD pattern of Fig. 2 because of the

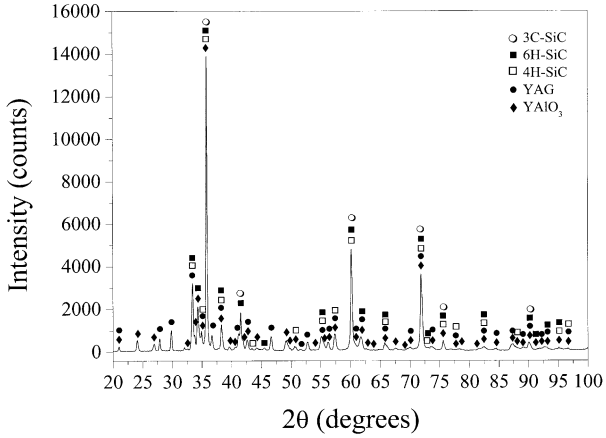

Fig. 2. X-ray diffraction pattern of the liquid-phase-sintered silicon SiC specimen showing the phase identification.

significant overlap of its Bragg reflections with those of the α-SiC polytypes. However, β-SiC was included in our phase-identification model and in our subsequent Rietveld refinement due to the following reasons: (1) β-SiC is the main constituent of the starting powders and, (2) there is a difference in the relative heights of the peaks at $2\theta = 35.6°$, 41.4°, 60.0°, 71.8°, 75.5° and 90.0°, which are 2θ positions attributed to the *fcc* crystallographic structure of the β-SiC polytype. The presence of the 4H, 6H as well as YAG and $YAlO_3$ phases means that during sintering the β→α polytype transformation occurred and that the Al_2O_3 and Y_2O_3 reacted to form the $Y_3Al_5O_{12}$ and $YAlO_3$. Both experimental facts are not surprising and they were already expected as β-SiC is known to be unstable at temperatures of >1600 °C in the presence of aluminum and as the $Y_3Al_5O_{12}$ and $YAlO_3$ are formed with the Y_2O_3:Al_2O_3 molar ratios of 3:5 and 1:1, respectively.

Now, we focus our attention on extracting a more detailed information from the diffractogram in Fig. 2. Thus, it is particularly relevant to determine accurately the relative amounts of the different phases that are present in the sample. For this purpose we have chosen the Rietveld method primarily due to inherent difficulty for determining accurately the sample composition (five phases and a significant overlap between their Bragg reflections). Fig. 3 shows the plotted output from the Rietveld analysis, where it is clear that exists an excellent agreement between the experimental XRD data and calculated XRD pattern using the Rietveld method. Thus, a careful visual examination of the difference plot in Fig. 3 shows that there is not any systematic difference between the observed and calculated patterns. In addition to this graphical criteria, the low value of the agreement indexes in Table 1 further reinforce that the fit is noticeably good, which in turn will allow us to extract valuable microstructural information from the fitted parameters.

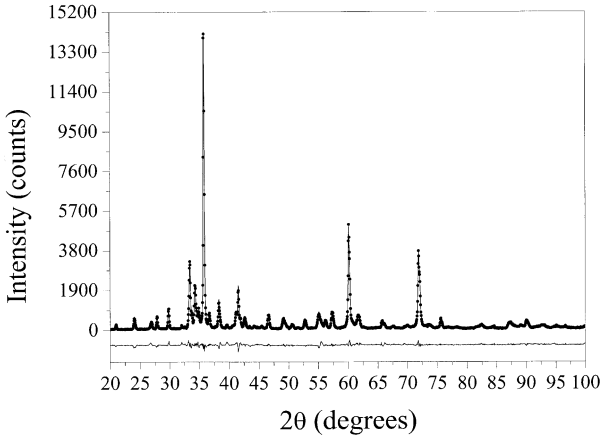

Fig. 3. Plot output from the Rietveld analysis of the X-ray diffraction pattern corresponding to the sintered sample. Points represent the experimental X-ray diffraction data and the solid line represents the calculated pattern. The difference plot is shown at the bottom.

Table 1
Rietveld analysis agreement indices and weight fractions of the different phases in the liquid-phase-sintered silicon carbide sample

Phase	Phase proportion (wt.%)
3C	48.7±0.8
6H	12.5±0.9
4H	13.3±0.6
$Y_3Al_5O_{12}$	16.4±0.3
$YAlO_3$	9.1±0.3
Agreement indices	
$R_{wp}=11.6$	
$\chi^2_r=3.9$	

The corresponding wt.% of the different phases in the sample are also presented in Table 1. Thus, the Rietveld refinement confirmed that the LPS SiC sample is primarily composed of the β-SiC polytype. This further reinforced our first observation of differences in the relative heights of the peaks at 2θ positions attributed to the XRD pattern of the β-SiC polytype. However, the metastable coexistence of β and α SiC polytypes is found in this study because the sintering time used was not enough for resulting in the termination of the β→α phase transformation. Despite the fact that there is not an independent evaluation of the composition determined in our study, there appears to be a close correspondence between the calculated phase-composition and that expected from the starting powders. For example, it is sufficient to consider that there is a favorable agreement between the 74.5±2.4 wt.% calculated here for all the SiC polytypes and the 73.86 wt.% SiC knew from the starting composition.

The Rietveld refinement used in this study also opens the possibility of carrying out an accurate microstructural analysis, which is the main objective of the present paper. Note that the Rietveld method is a powerful tool here because the individual overlapping Bragg reflections are resolved during the fit as all the lines for each phase are included explicitly in the refinement. Without this previous Rietveld refinement, the measurement of diffraction domain sizes has no sense at all. The application of the Rietveld method for the line-broadening study, being essential, is not evident as it is a whole pattern fitting procedure. It is essential as there is not other way of resolving the individual overlapping Bragg reflections, and its application is not trivial as it should keep in mind that the profile parameters obtained with the Rietveld method for a given phase represent the best profile parameters for all its set of *hkl* reflections. Of course, that does not mean that these are the best profile parameters for a particular *hkl* Bragg reflection, although it is evident that both must have closed values. Thus, a typical procedure for determining unambiguously the best profile parameters describing a particular experimental reflection would consist in modeling only its 2θ range by a more-detailed iterative fitting procedure; furthermore, the starting values for the fit should be those obtained in the Rietveld analysis. The use of this kind of soft or slack constraint (also known as restraint) is a key step for avoiding to achieve false minima when there is, like in our case, a severe overlap between different Bragg reflections.

In our case, we have selected the 2θ ranges containing the Bragg reflections 111 and 222 of the 3C polytype (that is, the intervals 35.2–36.4° and 74.5–76.2° 2θ) because we are interested in determining the crystallite size distribution of the β-SiC polytype along its crystallographic direction $<111>$. Fig. 2 shows that the peak located at $2\theta=35.7°$ is the overlap of the Bragg reflections 111-3C, 004-4H, 102-6H, 006-6H and 210-$YAlO_3$, while that located at $2\theta=75.5°$ is formed overlapping the Bragg reflections 222-3C, 008-4H, 0012-6H, 204-6H, 104-$YAlO_3$ and 332-$YAlO_3$. Also, the results obtained in the Rietveld analysis showed that the mayor contribution to these experimental peaks arises from the 3C polytype. However, the contribution from all the overlapping reflections has to be taken into account in the subsequent LM-fit if an accurate microstructural analysis is desired; otherwise, we would obtain a crystallite size distribution moved towards the left as compared with the real one. Fig. 4a and b show the plotted output from the LM-fit for the peaks at $2\theta=35.7°$ and $2\theta=75.5°$, respectively. Note the excellent agreement between the observed and calculated XRD data (see the difference plots in Fig. 4a and b as well as the agreement indexes in Table 2) and that the mayor contribution to the experimental intensities arises from the peaks of the 3C polytype. Also, Table 2 shows that, as already expected, there is a close correspondence between the Rietveld profile parameter values and those obtained

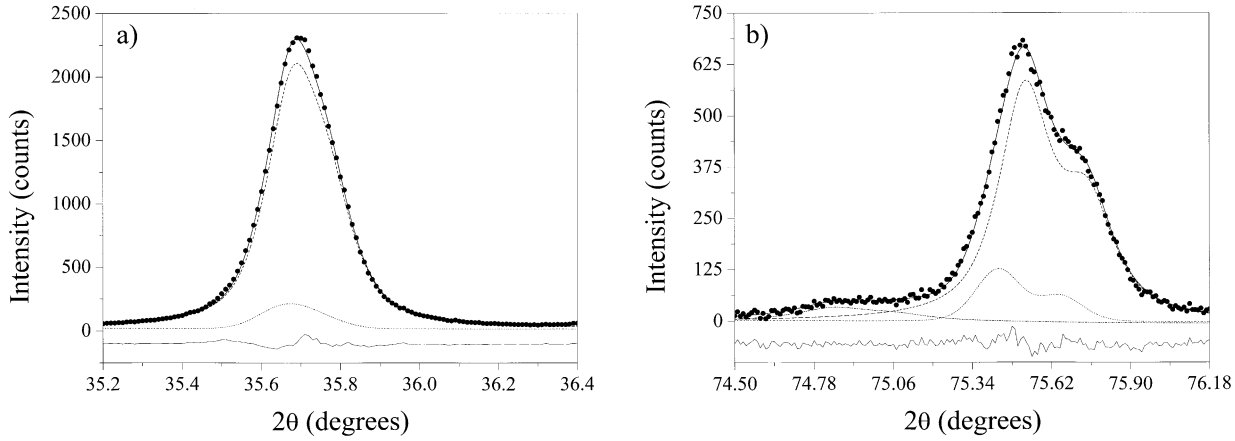

Fig. 4. Plot output from the Levenberg–Marquardt non-linear least-squares fit for the 2θ range containing the 111 (a) and 222 (b) experimental peaks of the 3C polytype. Points represent the experimental X-ray diffraction data and the solid line represents the calculated pattern (both corrected by the Lorentz-polarization factor). The difference plot is shown at the bottom. The contribution of the 3C polytype is shown by the dash line while the contribution arising from all the other phases is shown at one by the dot line. In the case (b), the dash-dot-dot line represents an independent group of peaks at $2\theta = 74.9°$.

Table 2
Starting Rietveld profile parameters, final profile parameters after the Levenberg-Marquardt non-linear least-squares fit and its corresponding agreement indices for the Bragg reflections 111 and 222 of the 3C polytype

Profile parameters	Bragg reflection 111		Bragg reflection 222	
	Starting profile parameters	Output profile parameters	Starting profile parameters	Output profile parameters
η	0.59	0.616	0.59	0.787
ω	0.0725°	0.0738°	0.1145°	0.1104°
$2\theta_0$	35.651°	35.677°	75.453°	75.526°
Agreement indices				
R_{wp}		3.1		3.5
χ^2_r		2.3		1.1

after the LM-fit. As mentioned in the fundamental concepts section, after resolving the experimental peaks of interest, an essential step for determining the unknown Fourier cosine transform $F_{hkl,C}(L)$ of the pure profile is an accurate knowledge of the instrumental-spectral contribution to the width and shape of these experimental profiles. For this reason, we have prepared an standard sample starting from a commercially available α-Al_2O_3 powder. The most important features in that α-Al_2O_3 standard sample is the coarse size for the crystallites and the absence of lattice microstrains; thus, the peak broadening arises exclusively from spectral and instrumental effects. Hence, we are faced with determining the profile parameters of the instrumental peaks; however, it should be borne in mind that there is no need for a previous Rietveld analysis here as: (1) we are dealing with just one phase; (2) the instrumental peaks

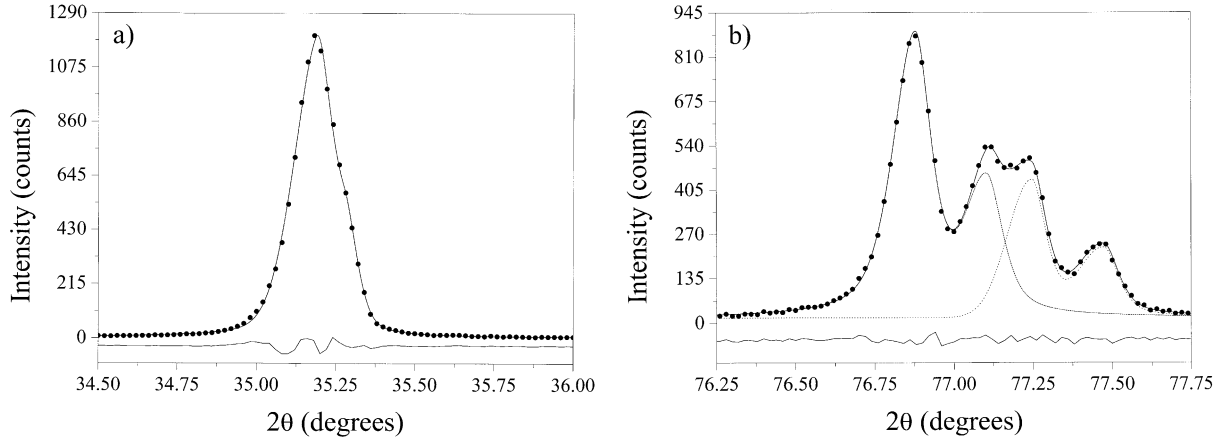

Fig. 5. Plot output from the Levenberg–Marquardt non-linear least-squares fit for the 2θ range containing the 104 (a) and 1010 (b) instrumental peaks of the the α-Al_2O_3 standard sample. Points represent the experimental X-ray diffraction data and the solid line represents the calculated pattern (both corrected by the Lorentz-polarization factor). The difference plot is shown at the bottom. In the case (b), the contribution of the 1010 Bragg reflection is shown by the dash line while that of the 119 Bragg reflection is shown by the dot line.

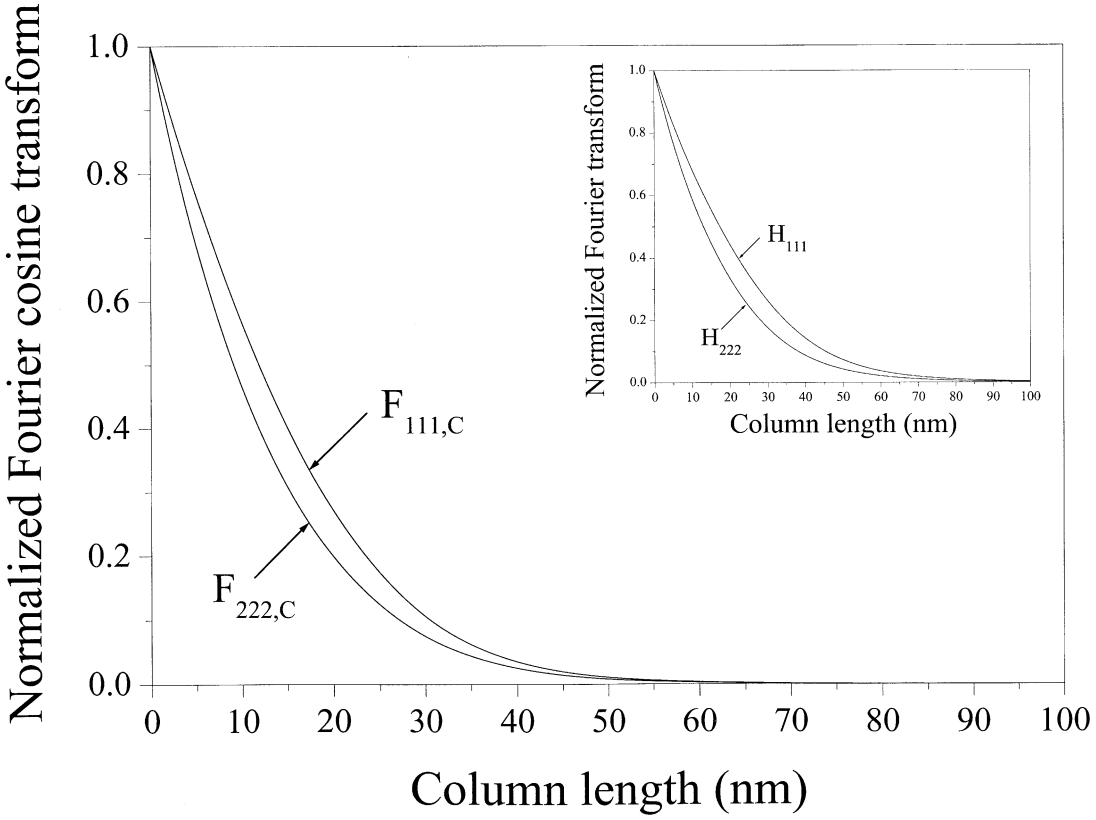

Fig. 6. Normalized Fourier cosine transform of the 111 and 222 pure Bragg reflections of the 3C polytype in the sintered sample. The normalized Fourier transforms of the corresponding experimental peaks are also shown in the inset.

are well-resolved and; (3) their starting values for the LM-fit can be easily obtained from a careful look to the XRD data. Fig. 5a and b show the plotted output from the LM-fit for the α-Al_2O_3 peaks at $2\theta = 35.2°$ (with Miller indexes 104) and $2\theta = 76.9$ (with Miller indexes 1010), respectively.[†] Again, the difference plots in Fig. 5a and b as well as the agreement indexes in Table 3 show the excellent agreement between the observed and calculated XRD data. For comparison, we have also included in Table 3 the profile parameters of both instrumental peaks. Note that Table 3 shows, as it has to be, that the instrumental peaks trend to be gaussian in the low 2θ range and lorentzian in the high 2θ range.

Once the profile parameters describing the two orders of the 111 Bragg reflection (peak 111-3C and 222-3C) and their corresponding instrumental peaks are accurately known, the microstructural characterization is straightforward. First at all, the four Fourier transforms [that is, $H_{111}(L)$, $H_{222}(L)$, $G_1(L)$ and $G_2(L)$] can be easily calculated from the analytical functions determined after the LM-fits. Now, the application of the Fourier integral-convolution theorem allows us to determine the Fourier cosine transforms of the pure profiles for both the 111 [$F_{1,C}(L)$] and 222 [$F_{2,C}(L)$] Bragg reflections of the 3C polytype. Fig. 6 shows the normalized Fourier cosine transforms $F_{1,C}(L)$ and $F_{2,C}(L)$ together with the normalized Fourier transforms $H_{111}(L)$ and $H_{222}(L)$ (inserted). Note that F_C(L) decreases faster than H(L) when L increases because the experimental peaks are broader than the pure peaks. Most importantly, Fig. 6 shows than $F_{1,C}(L)$ and $F_{2,C}(L)$ are evidently different

Table 3
Profile parameters after the Levenberg-Marquardt non-linear least-squares fit and its corresponding agreement indices for the Bragg reflections 104 and 1010 of the α-Al_2O_3 standard sample

Profile parameters	Bragg reflection 104	Bragg reflection 1010
	Output profile parameters	Output profile parameters
η_{Left}	0.228	0.528
η_{Right}	0.361	0.637
ω_{Left}	0.0882°	0.036°
ω_{Right}	0.0488°	0.0588°
$2\theta_0$	35.184°	76.878°
Agreement indices		
R_{wp}	5.5	4.7
χ_r^2	2.1	1.1

[†] Note that these peaks were chosen as instrumental lines because, having an appreciable intensity, they are placed at 2θ positions near to those of the 111 and 222 Bragg reflections of the β-SiC polytype.

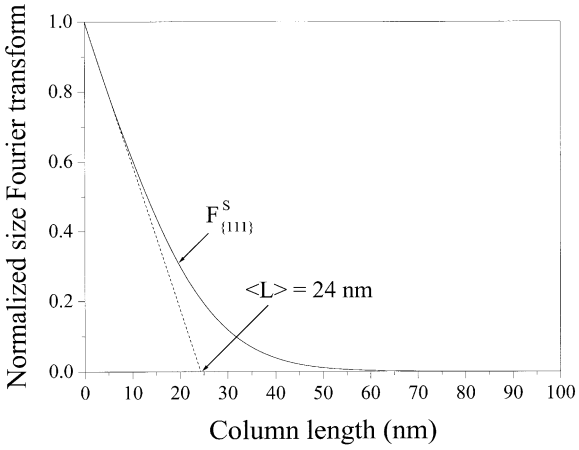

Fig. 7. Normalized size Fourier transform of the peaks corresponding to the {111} plane family of the 3C polytype in the sintered sample. A mean crystallite size of 24 nm is directly obtained from the abscissa intercept of the initial slope (dash line).

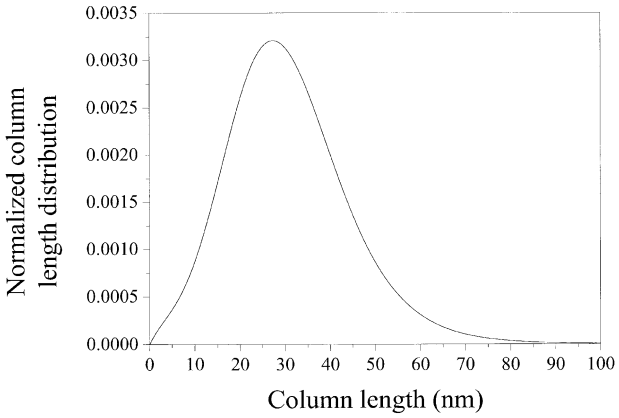

Fig. 8. Normalized crystallite size distribution along the crystallographic direction <111> of the 3C polytype in the sintered sample.

because, while having the same contribution from the crystallite size distributions, the contribution coming from the lattice microstrain distribution is not the same. Both $F_{1,C}(L)$ and $F_{2,C}(L)$, in conjunction with the interplanar spaces d_1 and d_2 is the only information needed for calculating, in a first step, $\sqrt{< e_L^2 >}$ according to the Eq. (8), and in a second step to separate the size and distortion components [$F^S_{\{hkl\}}(L)$ and $F^D_{hkl}(L)$, respectively] according to the Eq. (7). The component $F^S_{\{hkl\}}(L)$, that is, the normalized size Fourier transform is shown in Fig. 7. Note that $F^S_{\{hkl\}}(L)$ contains all the information regarding to the crystallite sizes. More specifically, the mean crystallite size can be directly obtained from the abscissa intercept of the initial slope and the crystal size distribution from the second derivative. Fig. 7 also shows that the average crystallite size along the crystallographic direction <111> of the β-SiC polytype obtained from the normalized size Fourier transform is 24 nm. It is worthy to mention that the mean crystallite size, which is an important microstructural parameter, can be more easily obtained using other alternative procedures as the mentioned variance and integral-breadth methods. Thus, the key feature of the Warren–Averbach method is its potential for providing the crystallite size distribution as the pure profile is restituted. Fig. 8 shows the column length distribution, again along the crystallographic direction <111> of the β-SiC polytype. It is important to note the there is not an appreciable presence of crystallites with sizes larger than 60 nm, that the maximum of that distribution is about 27 nm and that the distribution goes to zero at 100 nm. In other words, the β-SiC phase of the LPS SiC specimen can be considered as nanometric one. Both this nanostructured nature and the presence of α-SiC polytypes in the LPS SiC sample are in some way related to the stacking faults and microtwins in the SiC starting powders. With regards to these last points, it should be borne in mind that the difference between a highly twinned β-SiC structure (which is the case of our β-SiC starting powder as illustrated in Fig. 1a and b) and the structure of the different α-SiC polytypes is the periodicity of the stacking faults. Thus, the planar defects present in the SiC starting particles result in pseudo-localized regions of α-SiC. As already shown in others recent works,[15,16] in the initial stages of coarsening, α-SiC nucleates within the β-SiC starting particles and grows by both solution-reprecipitation (Ostwald ripening) and solid-state diffusion; this nucleation is believed to take place heterogeneously at coherent twin boundaries, at stacking faults and/or microtwins within the β-SiC starting particles because these planar defects already resemble local regions of α-SiC, therefore, facilitating easy nucleation. This could explain the presence of α-SiC after sintering for 0.5 h. Here we have focused now our interest in the solid-state diffusion as the crystallographic direction chosen for calculating the crystallite size distribution was the <111> of the 3C polytype. After the nucleation of the α-SiC lamellae, growth of these thin α-SiC regions consuming the faulted β-SiC regions could occur by propagation of suitable partial dislocations parallel to the β–α interfaces, the decreases in free energy being the driving force for such motion. However, the sintering time used in this study was not sufficient for the ending of that thickening stage and, therefore, the heavily faulted β-SiC regions could not be totally consumed. This could explain the nanometric nature of the diffraction domain size distribution determined using the Warren–Averbach method for the 3C polytype and its corresponding phase proportion of 48.7±0.8 wt.% determined using the Rietveld method. Then, it is argued that the so-formed β–α SiC composite grains still contain β-SiC regions highly faulted.

Finally, Fig. 9 shows the root-mean-square strain (along the crystallographic direction <111>) averaged over the column length L for the β-SiC polytype in the LPS SiC sample. Note that the plot of $\sqrt{< e_L^2 >}$ versus L

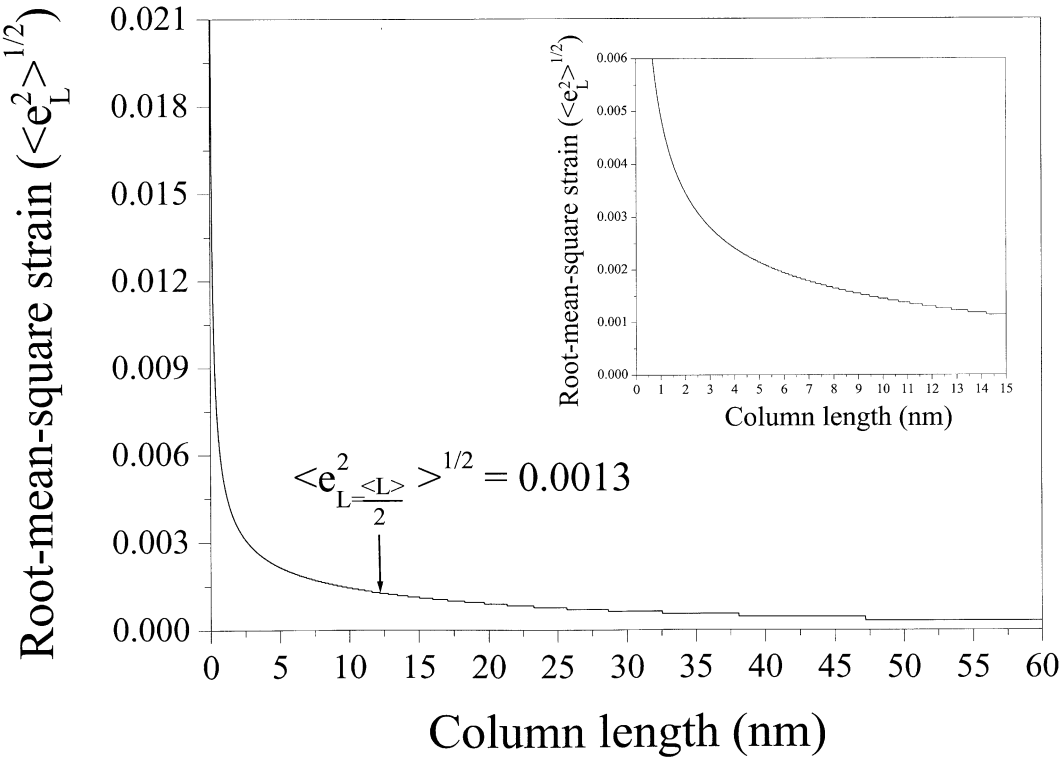

Fig. 9. Root-mean-square strain averaged over the distance L perpendicular to the diffracting {111} planes of the 3C polytype in the sintered sample. A magnification of low L range is also shown in the inset. A mean root-mean-square strain of 0.0013 is directly obtained from the ordinate at abscissa equal to the half of the mean crystallite size.

goes also to negligible values at $L \approx 60$ nm. These strains represent the distortions in the lattice parameters of the β-SiC polytype, probably due to its inherently faulted nature. In addition, the low value (0.0013) obtained in this study for the root-mean-square strain (usually calculated at L equal to the half of mean crystallite size, that is, at 12 nm in this study) is a consequence of the heat treatment at a temperature of 1950 °C, which induces the relaxation of the microstrains present in the crystallites of the β-SiC starting powders.

To conclude, we would like to remark that we have applied both the Rietveld and the Warren–Averbach methods to obtain some insights about the solid-state transformation within the SiC grains. An extension of this procedure to others crystallographic plane families could provide clouds about the lengthening of these grains, that is, about their growth by the solution-reprecipitation mechanism. In addition, the same procedure could be applied to follow the evolution of the α-SiC polytypes.

5. Summary

The feasibility of using the Warren–Averbach method in conjunction with the Rietveld method for the XRD characterization of LPS SiC ceramics has been demonstrated. The Rietveld method has been proved to be a valuable tool for obtaining, firstly, the phase composition and, secondly, the starting profile parameters for a more detailed line-broadening analysis. Subsequently, a LM-fit would resolve unambiguously the overlapping Bragg reflections. Finally, the Warren–Averbach method can be used for an accurate determination of the mean crystallite size, the crystallite size distribution and the averaged root-mean-square strain along a given crystallographic direction of any phase in the material. In the case of LPS SiC ceramics, the proposed procedure is specially useful due to the significant overlap between the Bragg reflections from both the different SiC polytypes and the sintering additives. It is also suggested that a systematic use of this methodology in samples sintered at different times could also contribute to a better understanding of the microstructural evolution in these technologically attractive and scientifically challenging ceramics.

Acknowledgements

The authors thank Mrs. H. Xu and Professor Nitin P. Padture at the University of Connecticut (USA) for their experimental assistance. Financial support of the Ministerio de Ciencia y Tecnología (Government of Spain) and Fondo Europeo de Desarrollo Regional (FEDER) under Grant No. CICYT MAT 2001–0799 is greatly appreciated.

References

1. Ortiz, A. L., Cumbrera, F. L., Sánchez-Bajo, F., Guiberteau, F., Xu, H. and Padture, N. P., Quantitative phase-composition analysis of liquid-phase-sintered SiC using the Rietveld method. *J. Am. Ceram. Soc.*, 2000, **83**(9), 2282–2286.
2. Ortiz, A. L., Cumbrera, F. L., Sánchez-Bajo, F., Guiberteau, F. and Caruso, R., Fundamental parameters approach in the Rietveld method: a study of the stability of results versus the accuracy of the instrumental profile. *J. Eur. Ceram. Soc.*, 2000, **20**(11), 1845–1851.
3. Ortiz, A. L., Cumbrera, F. L., Sánchez-Bajo, F., Guiberteau, F., Xu, H. and Padture, N. P., Aplicación del Método de Rietveld al Análisis Cuantitativo en SiC Sinterizado en Fase Líquida. *Bol. Soc. Esp. Ceram. Vidrio*, 2000, **39**(3), 347–350.
4. Ortiz, A. L., Sánchez-Bajo, F., Padture, N. P., Cumbrera, F. L. and Guiberteau, F., Quantitative polytype-composition analyses of SiC using X-ray diffraction: a critical comparison between the polymorphic and the Rietveld methods. *J. Eur. Ceram. Soc.*, 2001, **21**(9), 1237–1248.
5. Ortiz, A. L., Sánchez-Bajo, F., Cumbrera, F. L. and Guiberteau, F., X-ray powder diffraction analysis of a silicon carbide-based ceramic. *Mat. Lett.*, 2001, **49**(2), 137–145.
6. Rietveld, H. M., A profile refinement method for nuclear and magnetic structures. *J. Appl. Cryst.*, 1969, **2**, 65–71.
7. Young, R. A., *The Rietveld Method*. Oxford University Press, Oxford, 1993.
8. Warren, B. E. and Averbach, B. L., The effect of cold-work distortion on X-ray pattern. *J. Appl. Phys.*, 1950, **21**, 595–599.
9. Klug, H. P. and Alexander, L. E., *X-Ray Diffraction Procedures for Polycrystalline and Amorphous Materials*. John Wiley and Sons, New York, 1974.
10. Hill, R. J. and Howard, C. J., Quantitative phase analysis from neutron powder diffraction data using the Rietveld method. *J. Appl. Cryst.*, 1987, **20**, 467–474.
11. Bish, D. L. and Howard, S. A., Quantitative phase analysis using the Rietveld method. *J. Appl. Cryst.*, 1988, **21**, 86–91.
12. Hill, R. J., Expanded use of the Rietveld method in studies of phase abundance in multiphase mixtures. *Powder Diffr.*, 1991, **6**(2), 74–77.
13. Caglioti, G., Paoletti, A. and Ricci, F. P., Choice of collimators for a crystal spectrometer for neutron diffraction. *Nucl. Instrum. Methods*, 1958, **3**, 223–228.
14. Pujar, V. V. and Cawley, J. D., Computer simulations of diffraction effects due to stacking faults in β-SiC: I, simulation results. *J. Am. Ceram. Soc.*, 1997, **80**(7), 1653–1662.
15. Xu, H., Bhatia, T., Deshpande, S. A., Padture, N. P., Ortiz, A. L. and Cumbrera, F. L., Microstructural evolution in liquid-phase-sintered SiC: part I, effect of starting powder. *J. Am. Ceram. Soc.*, 2001, **84**(7), 1578–1584.
16. Deshpande, S. A., Bhatia, T., Xu, H., Padture, N. P., Ortiz, A. L. and Cumbrera, F. L., Microstructural evolution in liquid-phase-sintered SiC: part II, effect of planar defects and seeds in the starting SiC powder. *J. Am. Ceram. Soc.*, 2001, **84**(7), 1585–1590.